Automated Lung Segmentation in Digitized Posteroanterior Chest Radiographs[1]

Samuel G. Armato III, PhD, Maryellen L. Giger, PhD, Heber MacMahon, MD

Rationale and Objectives. The authors developed and tested a gray-level thresholding-based approach to automated lung segmentation in digitized posteroanterior chest radiographs.

Materials and Methods. Gray-level histogram analysis was initially performed to establish a range of thresholds for use during an iterative global gray-level thresholding technique. Local gray-level threshold analysis was then performed on the output of global thresholding. The resulting contours were subjected to several smoothing processes, including a rolling-ball technique. The final contours closely approximated the boundaries of the aerated lung regions. The method was applied to a database of 600 posteroanterior chest images. Radiologists rated the accuracy and completeness of the contours with a five-point scale.

Results. Results of the subjective rating evaluation indicated that this method was accurate, with 79% of the assigned ratings reflecting moderately or highly accurate segmentation and only 8% of the ratings indicating moderately or highly inaccurate segmentation.

Conclusion. This gray-level thresholding-based approach provides accurate automated lung segmentation in digital posteroanterior chest radiographs.

Key Words. Computers, diagnostic aid; images, processing; lung, radiography; radiography, digital.

Acad Radiol 1998; 5:245-255

[1] From the Department of Radiology, MC 2026, Kurt Rossmann Laboratories for Radiologic Image Research, University of Chicago, 5841 S Maryland Ave, Chicago, IL 60637. Received September 15, 1997; accepted October 13. Supported in part by U.S. Public Health Service grants CA48985 and T32 CA09649. **Address reprint requests to** S.G.A.

M. L. Giger and H. MacMahon are shareholders in R2 Technology, Inc (Los Altos, Calif). It is the University of Chicago Conflict of Interest Policy that investigators disclose publicly actual or potential significant financial interest which would reasonably appear to be directly and significantly affected by the research activities.

The utility of image-processing techniques in diagnostic chest radiology has increased with the growing acceptance of digital radiography, including both direct digital acquisition and conventional film acquisition with subsequent digitization (1). Methods of image enhancement, such as density correction and unsharp masking (2), have been used to reduce variations in the quality of bedside chest radiographs and to reduce the number of repeat examinations necessary because of exposure errors (3). Image data compression, image transfer protocols, digital archiving strategies, and interactive display consoles are being developed for use with picture archiving and communication systems, or PACS (4).

Various image-processing methods are being assimilated into computer-aided diagnostic, or CAD, schemes (5). Such schemes have been developed for the detection of lung nodules (6–11), interstitial infiltrates (12–14), pneumothoraces (15), cardiomegaly (16,17), and interval change (18).

Isolation of the lung regions in digitized chest radiographs, which is necessary for all these schemes, has been achieved through automated detection of the intercostal spaces (19), the rib borders (20–22), the rib-cage edge (23), and the complete lung boundary (24,25). To detect intercostal spaces, Powell et al (19) used vertical gray-level profiles, to which shift-variant sinusoidal functions were fit. Sanada et al (21) used a similar method to detect posterior rib borders. Statistical analysis of edge gradients and their orientations was then performed within small regions of interest (ROIs) to detect subtle continuous rib edges. Wechsler and Sklansky (20) fit linear, parabolic, and elliptic curve segments to the output of gradient and threshold operators to delineate the boundaries of anterior and posterior ribs. Chen et al (22) used edge-gradient analysis to determine whether ROIs used for lung-texture analysis overlapped rib edges. Xu and Doi (23) analyzed the first and second derivatives of gray-level profiles to delineate the rib-cage edge. Polynomial functions were then fit to initially detected edges. Cheng and Goldberg (24) applied a clustering algorithm to the gray-level histogram computed from a selected region of an image to identify a single gray-level threshold for lung segmentation. The resulting borders were then refined by means of linear and parabolic curve-fitting techniques. Pietka (25) delineated lung borders using a single threshold determined from the gray-level histogram of a selected region. Gradient analysis was then used to extend the edges.

Others have directly investigated the segmentation of lung regions for the detection of abnormal asymmetry (26), for the development of radiographic equalization techniques (27), for use with region-specific display-enhancement techniques (28–30), or for registering radiographs with radionuclide lung scan images (31). Duryea and Boone (27) devised a lung-segmentation method based on gray-level profiles and contrast information. To selectively enhance the mediastinum and subdiaphragm, Sherrier and Johnson (28) applied histogram-equalization techniques to areas determined by means of local gray-level histogram analysis to be within these regions. Sezan et al (29) identified in the gray-level histogram a lung-mediastinum threshold that could be used to perform adaptive unsharp masking in these different anatomic regions. McNitt-Gray et al (30) developed a pattern-classification scheme that implemented stepwise discriminant analysis as a basis for feature selection, which was then used to train classifiers. Clearly, automated segmentation of the lungs in chest images has many practical applications in addition to its role as a foundation for various computer-aided diagnostic schemes.

Therefore, we have developed a fully automated approach to lung segmentation in digitized posteroanterior (PA) chest radiographs. Gray-level thresholding forms the basis for this technique (32). The strength of this approach is that minimal a priori information about the location and morphology of the lungs in the image is needed; the contours defined during segmentation effectively expand to encompass the aerated portion of the lung regions. Consequently, this segmentation method is robust with regard to the overall morphology of the chest, even in the presence of severe radiographic abnormalities. In this study, we evaluated the performance of the lung segmentation method in the task of delineating the aerated lung regions in PA chest images.

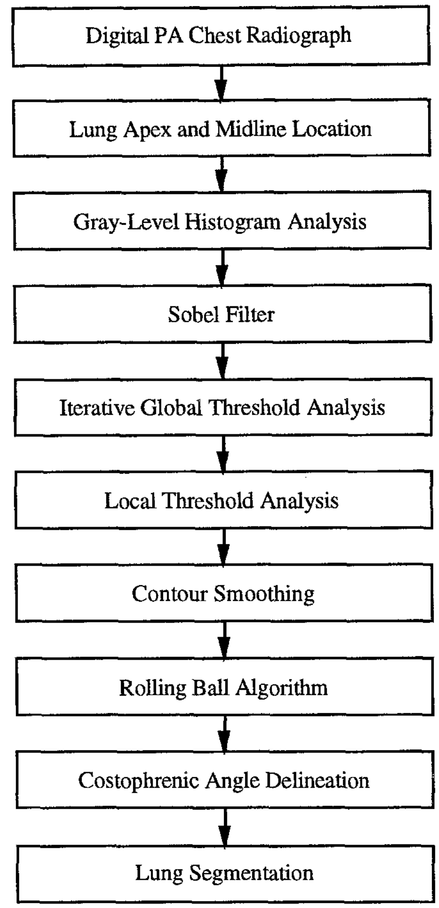

Figure 1. Overall scheme for automated segmentation of the aerated lung regions in digital chest radiographs.

MATERIALS AND METHODS

Database

An initial segmentation method that was developed based on a database of 70 PA chest images has been previously reported in the context of detection of abnormal asymmetry (26). The technique described herein incorporates substantial improvements over our initial method. We expanded the database to include a total of 118 images (18,33) (the "initial" database). After the method was completely developed with this initial database, an expanded database of 600 PA chest images was used for testing (23). Several broad classes of segmentation problems were identified and corrected based on findings from the first 300 of these images. The 600-image database was not completely independent of the training database, because the 600 images included the 118 initial images.

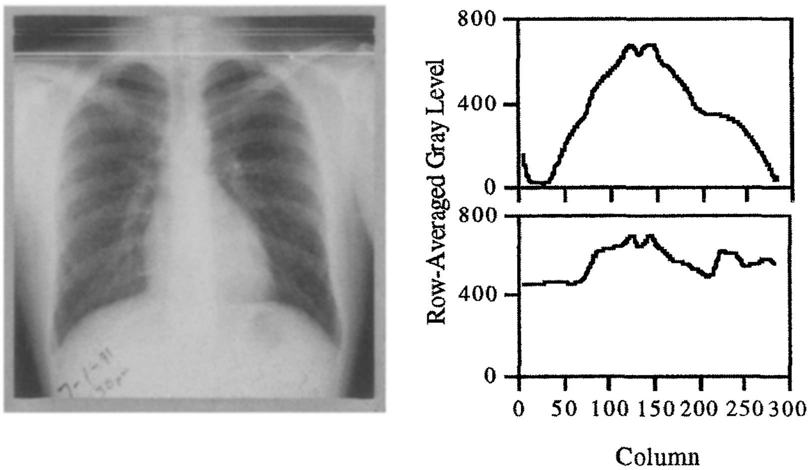

Figure 2. Demonstration of lung apex and midline determination. Row-averaged horizontal gray-level profiles from two sets of five consecutive rows are shown for a normal PA chest radiograph. The computer-determined lung apex and midline positions are indicated by the bright horizontal line and the vertical line segment, respectively.

All radiographs included in the various stages of the database were acquired at the University of Chicago (Ill) Hospitals. Radiographs of patients were acquired with 14 × 17-inch (36 × 43-cm) vertically oriented film. The radiographs were then digitized with a laser film scanner (KFDR-S; Konica, Tokyo, Japan), which assigns low gray levels to regions of high optical density and high gray levels to regions of low optical density, with 10-bit gray-scale quantization capable of producing a 2,000 × 2,500-pixel matrix (0.175-mm pixel size). Since it was empirically determined that such high resolution was not necessary for this type of segmentation task, all the images were reduced to a matrix size of 286 × 347 pixels (1.2-mm pixel dimension).

Overview

Figure 1 schematically outlines the computerized method for automated segmentation of aerated lung regions in PA chest images. The first step is to construct a gray-level histogram from a large rectangular ROI located near the central portion of the image. The maxima and minima of this histogram are analyzed to identify a range of gray levels that will be used during the iterative global gray-level thresholding process. Seven iterations are performed with progressively larger gray-level thresholds from the identified gray-level range (26). At each iteration, a binary image is constructed in which only pixels that have a corresponding image-pixel gray level less than the threshold are turned "on." An eight-point connectivity scheme is used to construct contours around each group of contiguous "on" pixels. Gray-level profiles constructed through the center of mass (centroid) of each such contour are analyzed to determine whether the contour encompasses pixels that belong to lung. Pixels in contours determined to be outside lung are prevented from contributing to binary images created at later iterations. A set of initial contours results after the seventh iteration. To capture the aerated lung region more completely, a local gray-level thresholding technique is implemented along the initial contours. A final contour set is constructed based on a composite binary image created by thresholding pixels within the individual local ROIs. The contours are smoothed, and a rolling-ball algorithm is used to eliminate large-scale irregularities in the contours. Lung segmentation is complete after application of a procedure for delineating the costophrenic angles.

Determination of Location of Patient Midline and Lung Apex

Horizontal gray-level profiles are analyzed to determine the location of the patient midline and the lung apices in each image. The midline position is used throughout the scheme to distinguish between right and left hemithoraces. The apex location effectively identifies an upper bound in the image above which no lung pixels are expected to exist.

A series of row-averaged horizontal gray-level profiles is constructed for the upper one-third of the image by considering groups of five rows at a time. The profiles are then analyzed for gray-level maxima and minima (Fig 2). Centrally located maxima are identified in each profile, which will contain either two such maxima if the trachea is prominent or a single maximum if it is not prominent. The midline position is defined as the average x position of all such maxima in all profiles.

The location of the lung apex is determined based on the profile minima. Although right and left lung apices

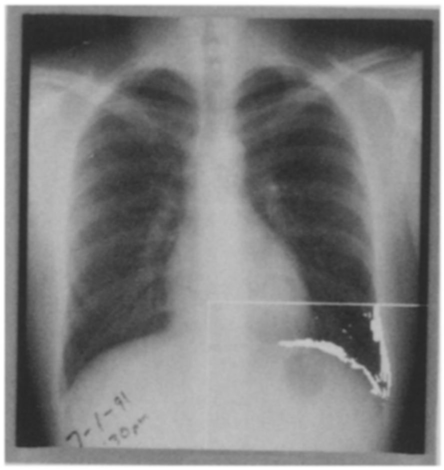

Figure 3. Image shown in Figure 2 after application of a Sobel filter to the lower right quadrant of the image. Filtered pixels with values that exceed a threshold are assigned a gray level of 999 in the image.

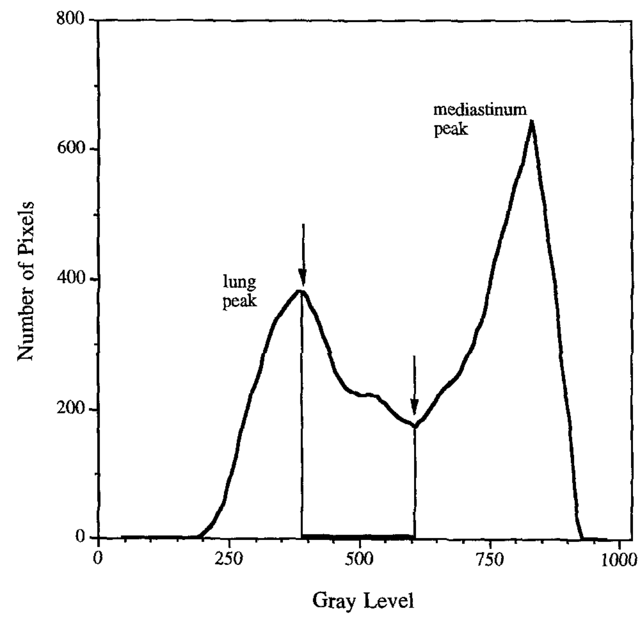

Figure 4. Typical global gray-level histogram that shows characteristic bimodal distribution. The arrows indicate the peak that contains pixels belonging predominantly to lung and the minimum between the lung and mediastinum peaks, respectively, as determined by the computer. This range represents the range of gray levels used in the iterative thresholding technique.

may occur at different rows as a result of patient rotation in the image plane, a single row that represents the more superior of the apices is identified to serve as an upper bound on the lung regions in the image. Consequently, the hemithoraces (now distinguished by the midline) are considered separately. The lowest minimum on each side of the midline is identified in all profiles, provided that the gray level of this minimum is between 15% and 85% of the central maximum gray level. This range was established by observing that a minimum below 15% is probably within the direct-exposure region, while a minimum above 85% represents a profile deviation that is too minor to consider. The lung apex is then identified as the row that corresponds to the first profile, such that the lowest minima of the succeeding (ie, inferior) two profiles have lower gray levels (Fig 2).

Iterative Global Gray-Level Thresholding

A Sobel filter (34) is convolved with the lower right quadrant of the image (ie, the patient's left side) to accentuate the diaphragm border and the lower rib-cage edge, thereby preventing the lung contours from incorporating radiolucent areas caused by bowel gas at higher gray-level thresholds. Pixels in the image quadrant that represent strong, appropriately directed gradients as determined by the filtered images are set to the arbitrary gray level 999 (Fig 3); this value is high enough to exceed any realistic threshold range identified through global gray-level histogram analysis. This enhancement acts as an artificial boundary that will not allow penetration of the left lung contour into the region occupied by bowel gas.

A global gray-level histogram is used to initiate the segmentation scheme. In an effort to obtain more uniform histograms, we limited the calculation of the histogram to a 181 × 141-pixel region centered 140 pixels from the top of the image—in other words, a region effectively centered over the thorax. A typical region will contain high-density (low gray level) pixels belonging to lung as well as low-density (high gray level) pixels that belong to more radiopaque structures such as the mediastinum, rib-cage edge, and diaphragm. Consequently, the histogram that results from such a region tends to be bimodal, with one peak centered over lower gray levels (the "lung peak") and another centered over higher gray levels (the "mediastinum peak") (Fig 4).

The goal of global gray-level thresholding is to use the histogram to determine an appropriate gray level that separates the gray levels that belong to pixels inside the aerated lung regions from those that belong to pixels outside the lungs. The task of determining an appropriate threshold based on a single gray level proved to be impossible. Either the values were too low and the resulting contours insufficiently captured the lung regions or the values were too high and the lung regions merged with

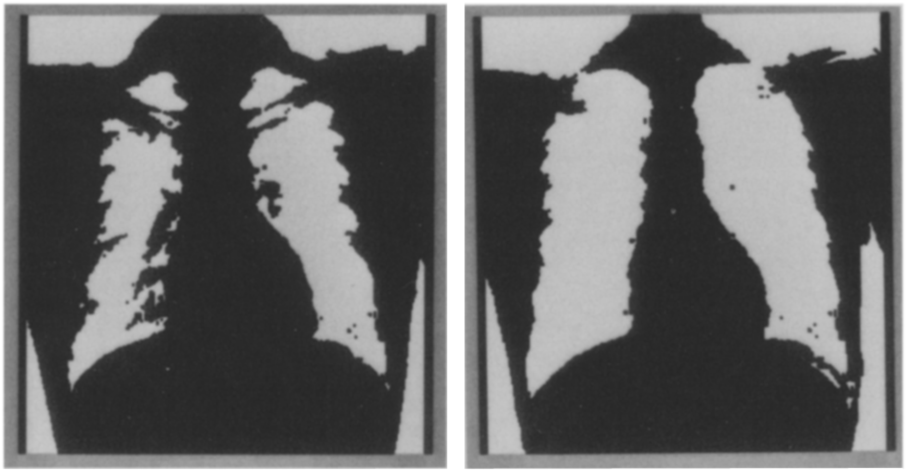

a. b.

Figure 5. Two binary images created by thresholding the image shown in Figure 2 at two different gray levels. The gray-level threshold used was lower in the construction of **(a)** than in **(b)**.

regions outside the lungs in a single contour. In most cases, a certain threshold value resulted in the former condition in one portion of the lung region and the latter condition in another portion (26).

Use of an iterative global gray-level thresholding scheme can overcome this problem. Instead of choosing one gray-level threshold value, one uses a range of values in succession (26). The slope of the global gray-level histogram is used to identify the gray level at which the lung peak occurs and the gray level at which the minimum between the lung and mediastinum peaks occurs (Fig 4). The iterative global gray-level thresholding technique then uses the range of gray levels bounded by these two points. The iterative process is defined by successive thresholding at seven equally spaced gray levels within this range.

A binary image is created during the first iteration by using the lowest of the seven gray levels (ie, the highest optical density of the range) as the threshold value. Pixels are turned "on" in the binary image if the corresponding pixel in the radiographic image has a gray level less than the threshold. This first threshold will obviously produce a binary image with fewer "on" pixels than any subsequent binary image. The resulting binary image is sent through a contour-detection routine, which uses an eight-point connectivity scheme to construct contours that represent the boundaries of groups of contiguous "on" pixels (35). The routine also calculates important geometric properties of these contours, such as the centroid of the contour, the compactness and length (in terms of pixels) of the contour, and the area enclosed within the contour (in terms of pixels) (36). Subsequent iterations create additional binary images based on successively larger gray-level thresholds (Fig 5). Contours are again constructed around regions of contiguous "on" pixels, and geometric parameters of each contour are calculated.

The iterative aspect of this process is crucial for proper lung segmentation. For any given threshold value, pixels that belong to the direct-exposure region outside the patient will be turned "on" in the binary image (because these pixels will have gray levels lower than the lowest gray-level threshold) along with pixels that belong to lung (the pixels of interest, which also possess typically low gray levels). Moreover, at intermediate threshold values, regions occupied by bowel gas, the trachea, portions of the shoulder, and subcutaneous tissue will also be turned "on." Consequently, unless pixels from these nonlung regions are suppressed, the contours around these regions will merge with the contours that encompass actual lung at the higher threshold values.

To prevent merging, a centroid check is performed for each contour constructed at each iteration. A horizontal gray-level profile is obtained through the image pixel that represents the centroid of the contour, extending from the midline column to the corresponding edge of the image. The positions and gray levels of maxima and minima relative to the position and gray level of the centroid pixel are used to assess whether the contour encompasses a region of the lungs. Depending on the location of the centroid, a vertical gray-level profile that begins at the centroid and extends to the top or bottom of the image is also analyzed to provide additional information about the region included within the contour. If the centroid check indicates that the contour exists outside the lung region, all image pixels enclosed by the contour are prohibited from contributing to the binary images (and hence the contours) created at later iterations (Fig 6). These external regions are thus prevented from merging with regions within the lungs at later iterations, during which the threshold gray level is greater and the likelihood of such a merge is increased. The lung contours that result from the higher threshold values used during later iterations are thus able to extend more toward the lung periphery without the risk of contours that would otherwise encompass nonlung regions "leaking through" the lung boundary to combine with the lung contour. This situation would typically occur along portions of the lung boundary that are more radiolucent, such as the inferior margins of the rib-cage edge and the left hemidiaphragm in the presence of bowel gas. Binary images created with (Fig 7a) and without (Fig 5b) implementation of the centroid check at earlier iterations are shown.

The process of using thresholding to create a binary image, identifying contours, and suppressing pixels based on a centroid check is repeated for each of the seven iterations; the threshold value used to produce the binary image is increased at each iteration. A morphologic open operation (34) with a 3 × 3-pixel kernel is applied to the binary images during each of the final three iterations. This combination of an erosion operation followed by a dilation operation eliminates many of the slender artifacts that remain "on" in the binary image as a result of the process that suppresses regions of the image based on the centroid check (Fig 7). The end result of the global gray-level thresholding scheme is an initial set of contours that represents the regions of aerated lung in the image (Fig 8a).

Contour Smoothing

Since the initial contours tend to appear somewhat irregular, a smoothing scheme is applied that uses a running mean algorithm. This algorithm substitutes for the x and y positions of each contour point the average x and y positions of nine preceding and nine succeeding contour points. In addition, points that are redundant in an eight-point connectivity sense are eliminated from the contours (Fig 8b).

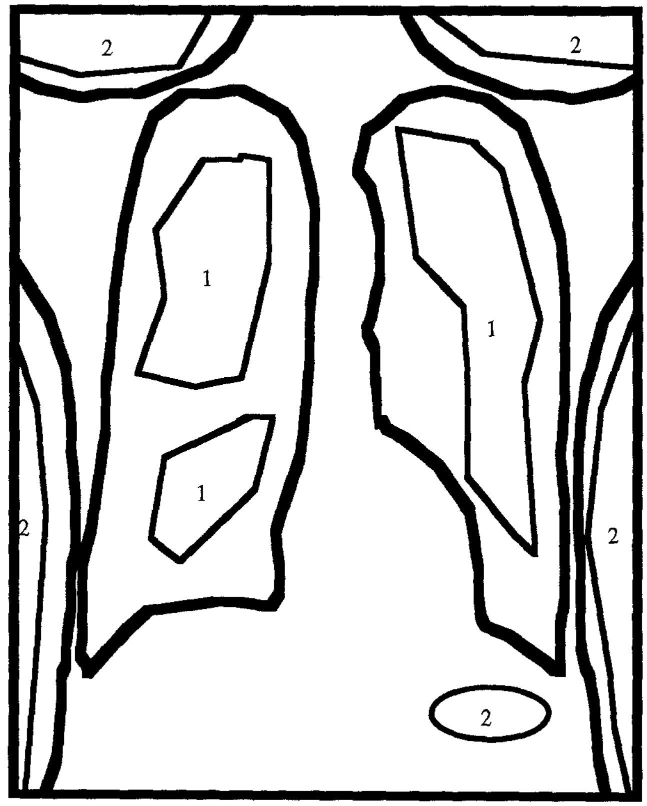

Figure 6. Schematic diagram of a chest image that shows contours detected during an intermediate iteration. Contours labeled *1* pass the centroid check. Contours labeled *2* fail the centroid check. Accordingly, pixels within these latter contours are prevented from being turned "on" during subsequent iterations.

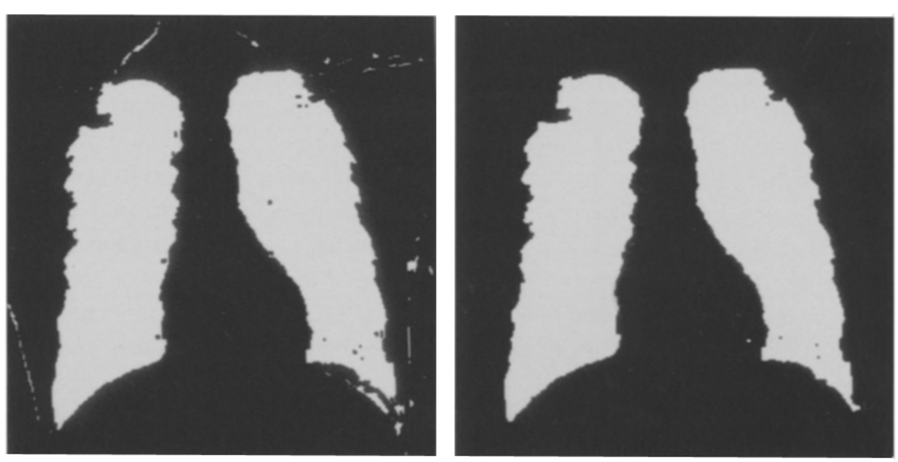

Figure 7. Binary images showing the effect of the centroid check. **(a)** This binary image is analogous to that shown in Figure 5b except that a centroid check has been performed during previous iterations. **(b)** The same binary image is shown after performance of a morphologic open operation to remove slender artifacts.

Local Gray-Level Thresholding

The initial contours determined based on global gray-level thresholding tend to underrepresent the actual aerated lung regions (Fig 8b). To rectify this situation, a local gray-level thresholding scheme is applied to the output of the global thresholding scheme. Overlapping ROIs that are 31 × 31 pixels (38 × 38 mm) in size are centered at every 30th pixel along the initial contours (Fig 9a). The dimensions of the ROI that are necessary to adequately perform local thresholding depend on the degree to which the contours that result from global thresholding approximate the actual lung borders. We selected a single ROI size (31 × 31 pixels) based on empiric observations of the initial contours.

Although all initial contours are retained, local thresholding is performed only on the two largest contours in the image, and then only if these contours occupy different hemithoraces. ROIs are assigned to one of two location categories (medial or lateral) as they are placed along the initial contours in a counterclockwise manner, beginning with the most superior point of each contour.

Gray-level analysis is performed on pixels within each ROI, and a gray-level threshold is determined separately for the individual ROIs based on their location categories. The threshold for a medial ROI is defined as the mean gray level of pixels within the ROI. For a lateral ROI, a gray-level histogram is constructed from all pixels within the ROI, and the initial threshold is set to the gray level at which the minimum with the largest gray level occurs (ie, the rightmost minimum in the histogram) (Fig 9a). The threshold actually used for a lateral ROI is the average of its initial threshold and that of the two adjacent ROIs. A composite binary image is then created by thresholding the pixels in each ROI based on the threshold value selected for that ROI such that a pixel is turned "on" in the binary image if its corresponding image pixel

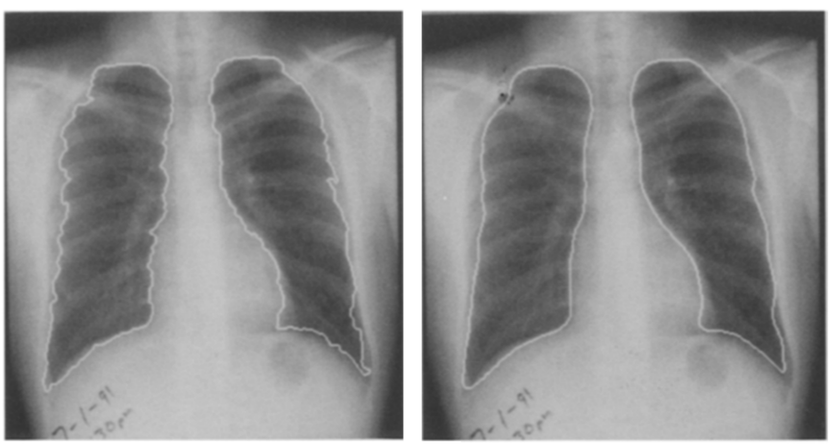

a. b.

Figure 8. Initial set of lung contours that resulted from iterative global gray-level thresholding for the image shown in Figure 2. The image is shown **(a)** before and **(b)** after smoothing. Note that portions of the contours are a substantial distance from the true lung borders.

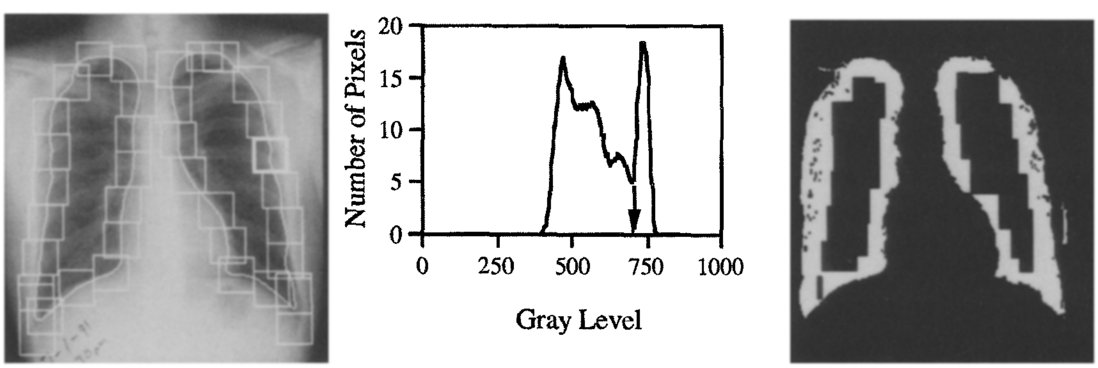

a. b.

Figure 9. Demonstration of local gray-level thresholding technique. **(a)** ROI placement along smoothed initial contours (Fig 8b) is shown. Larger ROIs overlap costophrenic angles. The gray-level histogram of the bolded ROI is shown and indicates its selected threshold. **(b)** Composite binary image created by thresholding pixels within individual ROIs is shown.

Figure 10. Final set of lung contours for the image shown in Figure 9a after local thresholding and smoothing.

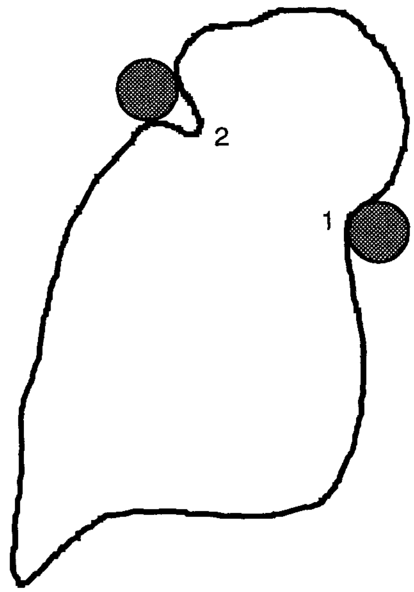

Figure 11. Illustration of rolling-ball algorithm for identifying depressions in a contour. The indentation at position *1* is not deep enough to qualify as a depression. Position *2* is considered a depression, however, because it prevents the ball from remaining in contact with the contour.

has a gray level less than the chosen threshold (Fig 9b). The contour-detection scheme is applied to the composite binary image to construct the final contours, which are then smoothed in the same manner as the initial contours previously discussed (Fig 10).

The final contours produced in this manner tend to underrepresent the costophrenic angles. To accommodate this important anatomic feature, an additional vertically oriented ROI (31 × 61 pixels) is placed over the initial contour point with the greatest distance from the opposite upper corner of the image. The average gray level of the pixels within this ROI is defined as the threshold, which is then used to create another portion of the composite binary image. This procedure is performed for each hemithorax.

Rolling-Ball Algorithm

The final contours sometimes contain large-scale aberrations, which appear as depressions or protrusions. These aberrations typically occur in the apex region, where a dense clavicle may cause the contour to bow inward to exclude the portion of the clavicle with the highest gray level, thus forming a depression in the contour. Alternatively, a relatively radiolucent region of the shoulder may erroneously be captured by the contour and may cause it to extend outward, thus forming a protrusion. The rolling-ball algorithm by Sternberg (37) was adapted to address this problem. The rolling ball is a spherical structuring element used to process images through gray-scale opening and closing operations. A ball is conceptually rolled along the three-dimensional surface that represents gray level as a function of spatial position in the image; filtering occurs where depressions exist in this surface that are sharp enough to prevent the ball of a specified radius from remaining in contact with the surface. The rolling ball we define analogously rolls along the two-dimensional curve defined by a lung contour. Depressions are identified where the rolling ball is unable to remain in contact with the contour (Fig 11). Applying the algorithm to the external side of the contour eliminates depressions, while applying it to the internal side eliminates protrusions, which appear to be depressions from this perspective.

Circular filters (the "ball") are constructed with radii that match the observed size of protrusions and depressions that tend to be present along the contours. Radii of 13 pixels (15.9 mm) for internal application and 25 pixels (30.6 mm) for external application were used in this study. The ball is "rolled" along the contour by successively identifying the pixel along the circumference of the ball which has a tangential slope that matches the slope of the current contour point; the filter is then positioned to align the selected ball-circumference pixel with the contour pixel. If a depression of the proper scale is encountered, the ball will overlap the contour at some contour point other than the point of contact used to place the filter (Fig 11). This overlap point along with the point of contact defines end points of the depression. Linear in-

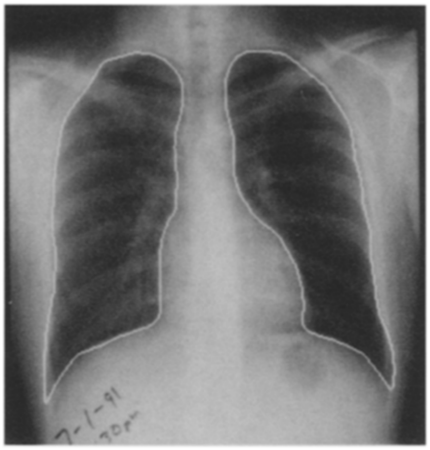

Figure 12. The final computer-determined contours overlaid on the normal PA chest image from Figure 2. These contours are the result of iterative global gray-level thresholding, local gray-level thresholding, smoothing, rolling-ball filtering, and costophrenic-angle delineation.

terpolation is then used to create new contour points that connect these end points to eliminate the depression.

Final Contour Delineation

The final contours are used to extract a 31 × 61-pixel subimage from each costophrenic-angle region. Gray-level analysis is performed within each row and column of the subimage to delineate the costal and diaphragmatic aspects, respectively, of the costophrenic angle. These delineations are then incorporated into the respective contours (38).

Figure 12 shows the normal PA chest image, used to illustrate the different aspects of the segmentation method, overlaid with the final computer-determined contours. These contours are the result of iterative global gray-level thresholding, local gray-level thresholding, smoothing, application of the rolling-ball filter, and delineation of the costophrenic angle. The contours for this image received a rating of 5 (highly accurate segmentation) from both radiologists during the subjective rating evaluation.

Subjective Rating Evaluation

The accuracy of the automated lung-segmentation scheme for PA chest images was assessed with the database of 600 PA chest images (286 × 347-pixel matrix). The scheme was applied to all cases, and the corresponding images with overlapping lung contours were printed on thermal paper with video printers (VP-3500 and VP-4500; Seikosha, Tokyo, Japan). The images were printed two per page, and each image was magnified by a factor of 2. A subjective rating evaluation of the computer-determined contours was then conducted with two attending radiologists. The observers were asked to rate the accuracy and completeness of the contours with a five-point scale, where 1 = highly inaccurate segmentation, 2 = moderately inaccurate segmentation, 3 = marginally accurate segmentation, 4 = moderately accurate segmentation, and 5 = highly accurate segmentation. Although the rating scale used was the same as the one implemented by Xu and Doi (23), observers in that study rated contours that resulted from the rib-cage edge-detection scheme, whereas the contours in the present study were rated for accuracy around the entire lung boundary. An important instruction given to the radiologists was that ratings assigned "should reflect your impression of the aerated lung region[s]," excluding "any [dense] pathology you interpret to be present," because the contours "are constructed to intentionally exclude dense anomalies in the images." They were explicitly told that "exclusion of pathology or medical devices [by the contours] should not negatively affect the assigned score," even though the "presence of external contours or contours that incorporate bowel or stomach gas" should influence the rating.

RESULTS

Figure 13 presents the results of the subjective rating evaluation. Figure 13a is a histogram of the scores assigned by the two radiologists individually, along with all 1,200 ratings considered together. Of all ratings, 79.1% (n = 949) reflected moderately or highly accurate segmentation (score of 4 or 5), and only 8.1% (n = 97, representing 65 different images) indicated one of the inaccurate categories (score of 1 or 2). The scores assigned were fairly consistent between the two radiologists; the most notable difference in Figure 13a is an apparent shift of some images from an assigned score of 5 by the first radiologist to an assigned score of 4 by the second radiologist. In fact, 69.5% (n = 417) of all 600 images received the same score from both observers. Differences between scores were greater than one for only 2.3% (n = 14) of the images, and most of these scores reflected the greater extent to which one observer penalized the segmentation when isolated contours were present outside the lungs or when small contours were constructed within the main lung contour.

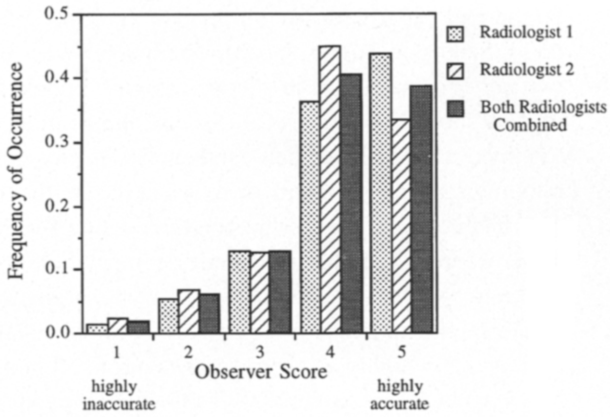

a.

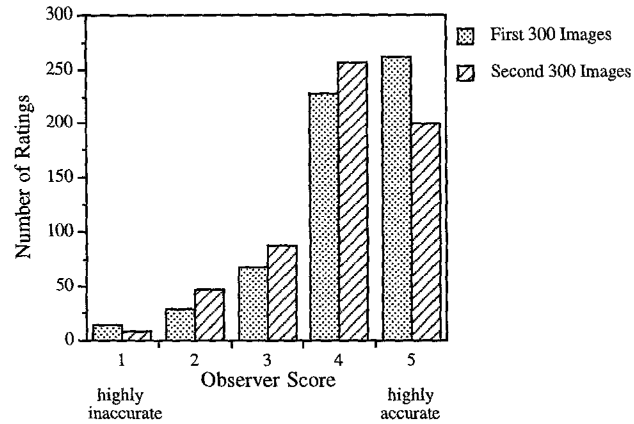

b.

Figure 13. Histograms display results of the subjective rating evaluation to assess segmentation accuracy for 600 PA images. **(a)** Radiologist ratings are presented individually and combined. **(b)** Segmentation accuracy ratings are presented for the first and second groups of 300 images.

Figure 13b presents a histogram of observer scores divided into two categories: ratings for the first 300 images (used to develop the automated segmentation scheme) and ratings for the second 300 images (an independent set). The second 300 images received fewer ratings of 5 than the first 300 images by a difference of 21.8%, although there was only a 6.7% difference between the image sets for ratings of 4 or 5 considered together. Accordingly, the second 300 images received more ratings of 2 and 3 than the first group. It is interesting to note that more images in the first group received a score of 1 than did images in the second group.

DISCUSSION

We have developed an automated method for segmenting the aerated lung regions in digitized PA chest radiographs. The accurate performance of this method has been demonstrated through a subjective rating evaluation. This approach to lung segmentation in PA chest images requires little a priori knowledge about overall lung morphology. Consequently, this method may be implemented as the first stage of various computer-aided diagnostic schemes designed to analyze diverse pathologic conditions.

ACKNOWLEDGMENTS

The authors express their appreciation to Steven Montner, MD, and Carl Vyborny, MD, PhD, for evaluating the segmentation contours and to Xin-Wei Xu, PhD, for his helpful discussions.

REFERENCES

1. MacMahon H, Doi K. Digital chest radiography. Clin Chest Med 1991; 12:19–32.
2. Yoshimura H, Xu XW, Doi K, et al. Development of a high quality film duplication system using a laser digitizer: comparison with computed radiography. Med Phys 1993; 20:51–58.
3. Hoffmann KR, Doi K, MacMahon H, et al. Development of a digital duplication system for portable chest radiographs. J Digit Imaging 1994; 7:146–153.
4. Huang HK, Taira RK. Infrastructure design of a picture archiving and communication system. AJR 1992; 158:743–749.
5. Giger ML, MacMahon H. Image processing and computer-aided diagnosis. Radiol Clin North Am 1996; 34:565–596.
6. Toriwaki J, Suenaga Y, Negoro T, et al. Pattern recognition of chest x-ray images. Comput Graphics Image Processing 1973; 2:252–271.
7. Hashimoto M, Sankar PV, Sklansky J. Detecting the edges of lung tumors by classification techniques. Proc IEEE Int Conf Patt Recogn 1982; 1801:276–279.
8. Lampeter WA, Wandtke JC. Computerized search of chest radiographs for nodules. Invest Radiol 1986; 21:384–390.
9. Giger ML, Doi K, MacMahon H. Image feature analysis and computer-aided diagnosis in digital radiography. III. Automated detection of nodules in peripheral lung fields. Med Phys 1988; 15:158–166.
10. Giger ML, Doi K, MacMahon H, et al. Pulmonary nodules: computer-aided detection in digital chest images. RadioGraphics 1990; 10:41–51.
11. Yoshimura H, Giger ML, Doi K, et al. Computerized scheme for the detection of pulmonary nodules: a nonlinear filtering technique. Invest Radiol 1992; 27:124–129.
12. Katsuragawa S, Doi K, MacMahon H. Image feature analysis and computer-aided diagnosis in digital radiography: detection and characterization of interstitial lung disease in digital chest radiographs. Med Phys 1988; 15:311–319.
13. Katsuragawa S, Doi K, MacMahon H. Image feature analysis and computer-aided diagnosis in digital radiography: classification of normal and abnormal lungs with interstitial disease in chest images. Med Phys 1989; 16:38–44.
14. Katsuragawa S, Doi K, MacMahon H, et al. Quantitative computer-aided analysis of lung texture in chest radiographs. RadioGraphics 1990; 10:257–269.
15. Sanada S, Doi K, MacMahon H. Image feature analysis and computer-aided diagnosis in digital radiography: automated

detection of pneumothorax in chest images. Med Phys 1992; 19:1153–1160.
16. Kruger RP, Townes JR, Hall DL, et al. Automated radiographic diagnosis via feature extraction and classification of cardiac size and shape descriptors. IEEE Trans Biomed Eng 1972; 19:174–186.
17. Nakamori N, Doi K, Sabeti V, et al. Image feature analysis and computer-aided diagnosis in digital radiography: automated analysis of sizes of heart and lung in chest images. Med Phys 1990; 17:342–350.
18. Kano A, Doi K, MacMahon H, et al. Digital image subtraction of temporally sequential chest images for detection of interval change. Med Phys 1994; 21:453–461.
19. Powell GF, Doi K, Katsuragawa S. Localization of inter-rib spaces for lung texture analysis and computer-aided diagnosis in digital chest images. Med Phys 1988; 15:581–587.
20. Wechsler H, Sklansky J. Finding the rib cage in chest radiographs. Pattern Recognition 1977; 9:21–30.
21. Sanada S, Doi K, MacMahon H. Image feature analysis and computer-aided diagnosis in digital radiography: automated delineation of posterior ribs in chest images. Med Phys 1991; 18:964–971.
22. Chen X, Doi K, Katsuragawa S, et al. Automated selection of regions of interest for quantitative analysis of lung textures in digital chest radiographs. Med Phys 1993; 20:975–982.
23. Xu XW, Doi K. Image feature analysis for computer-aided diagnosis: accurate determination of ribcage boundary in chest radiographs. Med Phys 1995; 22:617–626.
24. Cheng D, Goldberg M. An algorithm for segmenting chest radiographs. Proc SPIE 1988; 1001:261–268.
25. Pietka E. Lung segmentation in digital radiographs. J Digit Imaging 1994; 7:79–84.
26. Armato SG III, Giger ML, MacMahon H. Computerized detection of abnormal asymmetry in digital chest radiographs. Med Phys 1994; 21:1761–1768.
27. Duryea J, Boone JM. A fully automated algorithm for the segmentation of lung fields on digital chest radiographic images. Med Phys 1995; 22:183–191.
28. Sherrier RH, Johnson GA. Regionally adaptive histogram equalization of the chest. IEEE Trans Med Imaging 1987; MI-6:1–7.
29. Sezan MI, Tekalp AM, Schaetzing R. Automatic anatomically selective image enhancement in digital chest radiography. IEEE Trans Med Imaging 1989; 8:154–162.
30. McNitt-Gray MF, Huang HK, Sayre JW. Feature selection in the pattern classification problem of digital chest radiograph segmentation. IEEE Trans Med Imaging 1995; 14:537–547.
31. Armato SG III, Giger ML, MacMahon H, et al. Automated registration of ventilation/perfusion images with digital chest radiographs. Acad Radiol 1997; 4:183–192.
32. Armato SG III. Automated lung segmentation in digital posteroanterior and lateral chest radiographs: applications in diagnostic radiology and nuclear medicine. Dissertation. University of Chicago, Chicago, Ill, 1997.
33. Abe K, Doi K, MacMahon H, et al. Computer-aided diagnosis in chest radiography: preliminary experience. Invest Radiol 1993; 28:987–993.
34. Serra J. Image analysis and mathematical morphology. New York, NY: Academic Press, 1982.
35. Bae KT, Giger ML, Chen CT, et al. Automatic segmentation of liver structure in CT images. Med Phys 1993; 20:71–78.
36. Giger ML, Bae KT, MacMahon H. Computerized detection of pulmonary nodules in computed tomography images. Invest Radiol 1994; 29:459–465.
37. Sternberg SR. Grayscale morphology. Comput Vision Graphics Image Processing 1986; 35:333–355.
38. Armato SG III, Giger ML, MacMahon H. Computerized delineation and analysis of costophrenic angles in digitized chest radiographs. Acad Radiol (in press).